


## Article

# Exploration of Carbon Dioxide Curing of Low Reactive Alkali-Activated Fly Ash

Peyman Harirchi and Mijia Yang \* 

Department of Civil, Construction and Environmental Engineering, North Dakota State University, Fargo, ND 58104, USA; peyman.harirchi@ndsu.edu

\* Correspondence: mijia.yang@ndsu.edu

**Abstract:** In this paper, the effect of carbon curing procedure on low reactive fly ash alkali-activated pastes was investigated. Specimens were cured with pure carbon dioxide (CO<sub>2</sub>) gas for different curing times under 4 bar pressure. Chemical and physical characteristics of the geopolymer pastes were obtained from mass monitoring, titration test, XRD, FTIR and TGA-DTG analyses. Regarding the test results, after three days of CO<sub>2</sub> curing, the highest CO<sub>2</sub> uptake was obtained at 4.8 wt% of fly ash precursor, with carbon sequestration efficiency at 22.6%. The ratio of carbon dioxide absorbed as efflorescence to the total absorbed CO<sub>2</sub> was measured. The results show that at early age, almost 50% of carbonated products appeared as efflorescence; however, by increasing the curing time, and after 3 days of curing, about 80% of carbon dioxide was stored in the matrix. It was found that, in all cases, carbonation curing was detrimental to the geopolymerization process due to a high amount of efflorescence and led to a reduction in the compressive strength. At 24 h and 3 days, the specimens showed a lower reduction in compressive strength in comparison to CO<sub>2</sub> samples cured at 3 h, 6 h and 12 h. Regarding the XRD results, calcite was detected in the 24 h and 3 days specimens, which contributes to lower pore sizes due to a higher molar volume and production of silica gel that might participate in the polymerization processes and results in densified microstructures.

**Keywords:** carbon dioxide curing; alkali-activated material; fly ash; FTIR; efflorescence; XRD



**Citation:** Harirchi, P.; Yang, M. Exploration of Carbon Dioxide Curing of Low Reactive Alkali-Activated Fly Ash. *Materials* **2022**, *15*, 3357. <https://doi.org/10.3390/ma15093357>

Academic Editor: Jie Hu

Received: 3 April 2022

Accepted: 4 May 2022

Published: 7 May 2022

**Publisher's Note:** MDPI stays neutral with regard to jurisdictional claims in published maps and institutional affiliations.



**Copyright:** © 2022 by the authors. Licensee MDPI, Basel, Switzerland. This article is an open access article distributed under the terms and conditions of the Creative Commons Attribution (CC BY) license (<https://creativecommons.org/licenses/by/4.0/>).

## 1. Introduction

Due to calcination reaction of the carbonate minerals in cement manufacturing, the production of one tonne of cement approximately releases one tonne of carbon dioxide (CO<sub>2</sub>) [1]. Consequently, the cement industry has been responsible for almost 8% of CO<sub>2</sub> emissions in 2020; therefore, the reduction and control of CO<sub>2</sub> emission is becoming a major trend in the cement and concrete industry [2].

In recent years, CO<sub>2</sub> curing of fresh concrete as a carbon capture and storage (CCS) method has been adopted due to the urgency of CO<sub>2</sub> mitigation [3–5]. Using this technology, gaseous CO<sub>2</sub> is permanently fixed into thermodynamically stable minerals, such as calcium or magnesium carbonates [6,7], which leads to improvement of physical properties and durability of concrete [3,8]. The effect of carbon curing generally depends on the rate of CO<sub>2</sub> diffusion, carbonation rate, concentration of carbon dioxide, relative humidity and chemical composition of the mix [9–12]. The enhancement of the properties of final products is rooted in the quality and quantity of calcium carbonate generated in the pore structure in the early ages of hydration.

Pro-environment alternatives to the ordinary Portland cement (OPC) have been developed since 1940 called alkali-activated materials (AAMs) and geopolymer concrete (GC) [13]. AAMs are aluminosilicate industry byproducts, such as granulated blast furnace slag (GBFS) or fly ash (FA), which show cementitious properties by adding alkali solutions, such as sodium hydroxide (NaOH) and water glass [8]. The reaction forms a three-dimensional Si-O-(Si or Al) framework, and the final product contains sodium-aluminosilicate-hydrate (N-A-S-H) and calcium-aluminosilicate-hydrate (C-A-S-H) gels.

The resulting solid has a rapid strength gain, low permeability, high chemical, high heat resistance and low thermal conductivity, which make these materials qualified candidates for replacing OPC with a significant reduction in CO<sub>2</sub> [8,14–17].

The conventional curing methods of FA-based concrete are water curing and steam curing in which curing time and temperature are the most important factors for controlling the compressive strength [18]. Recent studies have investigated the effect of carbon dioxide curing on both OPC and AAMs for further reduction in CO<sub>2</sub> footprint. Zhang et al. investigated the effect of CO<sub>2</sub> curing on the pozzolanic reaction in fly ash concrete [7]. They found that if carbonation is limited to 12 h, it activates the fly ash OPC specimen at an early time of hydration, and the pH value of the pore solution is comparable to the control sample without the fly ash. Kassim et al. measured the effect of carbonation curing on the mechanical properties of alkali-activated electric arc furnace slag and reported a significant improvement of physical properties in CO<sub>2</sub> cured samples [19]. Park et al. examined the effect of CO<sub>2</sub> rich environment on FA-based alkali-activated materials with oven heating treatment [20]. They observed that the carbonated minerals densify the microstructure and improve the compressive strength of CO<sub>2</sub> cured samples. It was found that in CO<sub>2</sub> cured samples, the aluminosilicate gel contained a higher amount of silicates. Mei et al. investigated the mechanical and microstructure properties of alkaline-activated blast furnace slag (BFS) under accelerated carbonation [2]. They concluded that the carbonation of AAMs under a high CO<sub>2</sub> concentration deteriorates the matrix structure due to the consumption of Ca ions in C-S-H gel. Consequently, the resulting pores in carbonated specimens accelerate CO<sub>2</sub> diffusion and contribute to the weakening of the structure. Ohenoja et al. used peat-wood fly ashes from different sources for mineral carbonation [6]. The results showed an inconsistent effect of carbonation curing on the mechanical properties and a reduction in compressive strength in one fly ash sample, while in other samples, an increase in compressive strength was observed. Yamazaki et al. reported that in fly ash AAM, the N-A-S-H structure does not change with respect to accelerated carbonation [8]. Ul Haq et al. enhanced the fly-ash-based GC by in situ carbonation and reported that higher geopolymerization was achieved in the carbonated specimens [15]. Similarly, the polymerization effect of carbonation was reported by Nedeljkovic et al. [12].

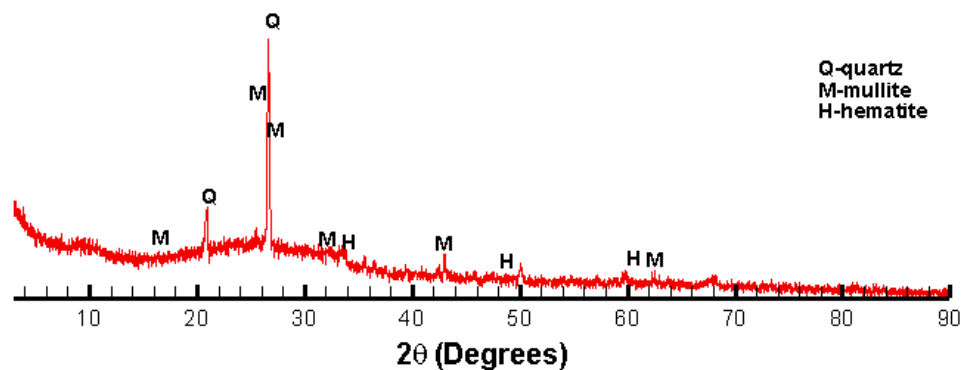
The effect of CO<sub>2</sub> on the geopolymerization process and the effectiveness of carbon mineralization require further investigation due to the inconsistency of reported results in the literature. Annually, large-volume fly ash fails to meet the requirements of national standards, such as ASTM C618, due to low reactivity [21]. In this paper, the effect of carbonation curing on alkali-activated pastes composed of low reactive fly ash without heat treatment is examined. The CO<sub>2</sub> mineralization capacity is measured through titration tests for specimens cured in a carbonation chamber under 4 bar pressure of pure CO<sub>2</sub>. The mechanical properties of these samples are then tested, and the effect of carbon curing is investigated by XRD, FTIR and TGA analyses.

## 2. Materials

The chemical composition of the fly ash used in this study is measured by a Rigaku Supermini 200 X-ray fluorescence spectrometer (Applied Rigaku Technologies, Inc., Austin, TX, USA) and shown in Table 1. The composition indicates that the fly ash contains high amounts of SiO<sub>2</sub>, Al<sub>2</sub>O<sub>3</sub> and CaO, and is categorized under type F regarding the ASTM C618-19 standard [22]. The basicity coefficient ( $K_b = \frac{\text{CaO} + \text{MgO}}{\text{SiO}_2 + \text{Al}_2\text{O}_3}$ ) and the hydration coefficient ( $H_M = \frac{\text{CaO} + \text{MgO} + \text{Al}_2\text{O}_3}{\text{SiO}_2}$ ) are calculated as 0.27 and 0.78, respectively. The majority minerals found by the X-ray diffraction test are quartz, mullite and hematite, as shown in Figure 1. The surface area calculated through the Brunauer–Emmett–Teller (BET) method is 0.5034 m<sup>2</sup>/g.

**Table 1.** Chemical composition of the used fly ash.

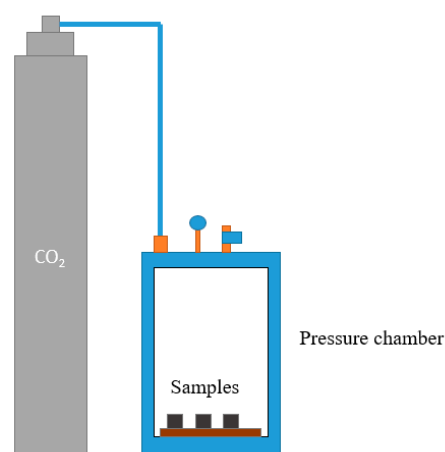
	CaO	SiO <sub>2</sub>	Al <sub>2</sub> O <sub>3</sub>	MgO	Fe <sub>2</sub> O <sub>3</sub>	TiO <sub>2</sub>	K <sub>2</sub> O	Na <sub>2</sub> O	Other
Fly ash	13.7	51.1	16.2	4.2	6.1	0.7	2.64	2.85	2.51

**Figure 1.** XRD results of the used fly ash sample.

The alkali activator used in this study is a mixture of sodium hydroxide (NaOH) with a purity of 98(%) and sodium silicate (Na<sub>2</sub>SiO<sub>3</sub>) solution with 9% Na<sub>2</sub>O and 28% SiO<sub>2</sub>. An amount of 5 M/L solution of NaOH is mixed with Na<sub>2</sub>SiO<sub>3</sub> solution in a way that the molar ratio of silicon oxide to sodium oxide equals 1 (SiO<sub>2</sub>/Na<sub>2</sub>O = 1). The alkali activator is prepared 24 h before being added to the fly ash precursor and kept at laboratory temperature.

### 2.1. Preparation of Samples and Experimental Set-Up

The water to binder ratio (*w/b*) is set to 0.3 for all samples. Besides the added water in the activator, water of the sodium silicate solution is considered in the calculation of water content. For each curing time, three samples are prepared. The compressive strength test is conducted with respect to ASTM C305-20 using 2-inch cubes [23]. After demolding, the samples are cured in the carbonation chamber under 4 bar pressure of 100% CO<sub>2</sub> in a set-up shown in Figure 2. Non-carbonation samples (NC) are cured in an ambient environment with 66% relative humidity (RH) at 22 °C temperature. The samples are cured for 3, 6, 12, 24 h and 3 days, and are named 3 h, 6 h, 12 h, 24 h and 3 days, respectively.

**Figure 2.** Carbon curing set-up.

### 2.2. Characterization Methods

#### 2.2.1. Mass Monitoring

For measuring CO<sub>2</sub> absorption, the mass monitoring method as a nondestructive method was adopted by previous researchers [24–27]. The key in measuring the CO<sub>2</sub> uptake

in carbonated samples is the estimation of water evaporation; therefore, a comparison between NC samples and carbonated samples is made for measuring the evaporable water. First, the water loss rate for NC samples (*WRNC*) is measured using Equation (1), and then, the change of mass with respect to CO<sub>2</sub> curing is calculated by assuming the same evaporable water content for the carbonated samples. Based on ASTM C566-19, the samples are heated in an oven at a temperature 110 ± 5 °C to measure the mass of evaporable water [28].

$$WRNC = \frac{M_1 - M_2}{M_1} \times 100 \quad (1)$$

In Equation (1), *M*<sub>1</sub> and *M*<sub>2</sub> are mass of a sample before and after oven heating, respectively. The mass of evaporable water (*M*<sub>w</sub>) in all samples is calculated using *WRNC* and the initial mass of a sample (*M*<sub>1</sub>) by applying Equation (2).

$$M_w = \frac{M_1 \times WRNC}{100} \quad (2)$$

The CO<sub>2</sub> uptake for carbonated samples is calculated using Equation (3) in which *M*<sub>b</sub> is the mass of fly ash used in each sample.

$$CO_2 \text{ uptake}(\%) = \frac{(M_2 + M_w) - M_1}{M_b} \times 100\% \quad (3)$$

### 2.2.2. Measurement of Absorbed CO<sub>2</sub>

One important issue in the implementation of geopolymer concrete is efflorescence on the surface of specimens. Unreacted alkali ions diffuse on the surface, react with CO<sub>2</sub> in the air and form white carbonates known as efflorescence [26]. The reduction in efflorescence can be investigated by the surface modification method [29], through the control of concrete microstructure and decrease in the fluidity of alkali [30]. Efflorescence can be evaluated in different ways, such as immersing the specimens in water and measuring the weight of dissolved salts after drying the solution [31]. In another method, the efflorescence image is captured using a camera and compared with Na<sup>+</sup> concentration at a different pH value of leachate [30]. However, the image-based method is not accurate because the efflorescence products include calcium and potassium cations in addition to sodium cations [26,32].

Additionally, the measurement of OH<sup>−</sup> and HCO<sub>3</sub><sup>−</sup> must be considered in the evaluation of efflorescence. Due to lack of efflorescence measurement standards in AAMs, the water immersion method is adopted in this study, since carbonation products, including sodium carbonates and bicarbonates, are soluble in water. After CO<sub>2</sub> curing, the samples are immersed in water for 2 days. In this process, water dissolves sodium carbonates and bicarbonates on the surface, but the calcium carbonate fixed in the matrix remains insoluble. The concentration of carbonate minerals in the solution is obtained by applying the titration test following the requirements of ASTM D3875-15 [33]. The ratio of CO<sub>2</sub> in the soluble products to the total CO<sub>2</sub> absorption shows the efficiency of carbonation curing.

### 2.2.3. Compressive Strength

The samples, with respect to different carbon curing durations, are tested by the universal compression testing machine. The low reactivity of fly ash indicates that only late-age compressive strength is detectable; therefore, a 28-day compressive strength is reported for all samples regarding ASTM C109/C109M [34]. For each CO<sub>2</sub> curing configuration, three samples are prepared, and the average compressive strength is plotted as a bar chart with the error bar representing the range of the strength variation.

### 2.2.4. X-ray Diffraction (XRD)

XRD diffractograms are conducted using Rigaku SmartLab (Applied Rigaku Technologies, Inc., Austin, TX, USA) for identification of minerals and phase changes of crystals in all samples [8]. XRD test shows the crystalline phases for samples with respect to different carbonation times. Different polymorphs of calcium carbonates could be detected at high

pressure of CO<sub>2</sub>. The peaks of calcium carbonates, including calcite (higher stability and crystallinity) and vaterite (lower stability and crystallinity), are expected in this experiment.

#### 2.2.5. Fourier Transform Infrared Spectroscopy (FTIR)

FTIR measures the absorption of infrared radiation by different functional groups; it identifies the molecular components and structures in the material [35]. FTIR is applied to specimens through the Thermo Scientific Nicolet 8700 FT-IR spectrometer (BRUKER, Allentown, PA) to monitor the change of the gel structure for different carbon-cured samples. FTIR is also conducted for measuring the reactivity of fly ash by the method proposed by Zhang et al. [36]. By deconvolution of the absorbance spectrum between 400 cm<sup>-1</sup> and 1400 cm<sup>-1</sup> band, the Gaussian curves corresponding to the active and inactive bonds are obtained. In the active bonds, Si and Al atoms are easily dissolved in the geopolymerization process. The active bonds are represented in Table 2. The relative area of convoluted bonds is assumed as an index of concentration of each bond. Since the solubility of active bonds is not equal, reactivity coefficients are applied to modify the contribution of each active bond. Regarding Ref [36], weaker bonds appear in the lower regions of the FTIR spectrum; consequently, reactivity coefficients for high to low regions are chosen as 0.25, 0.5, 0.75 and 2.

**Table 2.** FTIR range of active bonds in geopolymerization (adopted from Ref [36]).

Range	Bond Description
1085–1092	Asymmetric stretching of (Si, Al)-O-Si in glass phase, Q <sup>3</sup>
997–1011	Asymmetric stretching of (Si, Al)-O-Si in amorphous glass phase
900–915	Asymmetric stretching of Si-O <sup>M</sup> where M is an alkali metal
692–730	Symmetric stretching of Al-O in (Si, Al)-O-Al

#### 2.2.6. Thermogravimetric Analysis (TGA)

TGA is performed on all samples using TA Instrument Q500 to analyze their chemical compositions. The samples are heated with pure nitrogen gas from 25 °C to 1000 °C at the rate of 20 °C/min to quantify both carbonated and amorphous minerals.

### 3. Results and Discussions

The test results of the CO<sub>2</sub> cured samples are presented in this section. First, the reactivity of the fly ash samples is measured using FTIR, and then, the mechanical properties, including mass change, compressive strength and amount of CO<sub>2</sub> absorption, are presented. Next, spectroscopic results of the CO<sub>2</sub> cured samples and NC samples are demonstrated by XRD, FTIR and TGA.

#### 3.1. Quantitative Measurement of Reactivity of Fly Ash

Figure 3 shows the FTIR absorbance and Gaussian convoluted curves of the active bonds. It is assumed that the relative area of a resolved bond represents its concentration in the sample. The reactive surface area is calculated by multiplication of the active concentration by surface area obtained from the BET gas adsorption test. The relative area, reactive coefficient, active concentration and reactive surface area of the FA sample are shown in Table 3.

The active bond represents the Si-O-Al bond, which is easily broken in the presence of an alkali activator and dissolves at a faster rate in comparison to the inactive bonds. These bonds are mostly related to non-bridging oxygen with the Q<sup>3</sup>, Q<sup>2</sup>, Q<sup>1</sup> and Q<sup>0</sup> molecular structure [36]. The reactive surface value (0.144 m<sup>2</sup>/g), in comparison to the values reported in Ref [36], indicates low reactivity of the FA sample in this study.

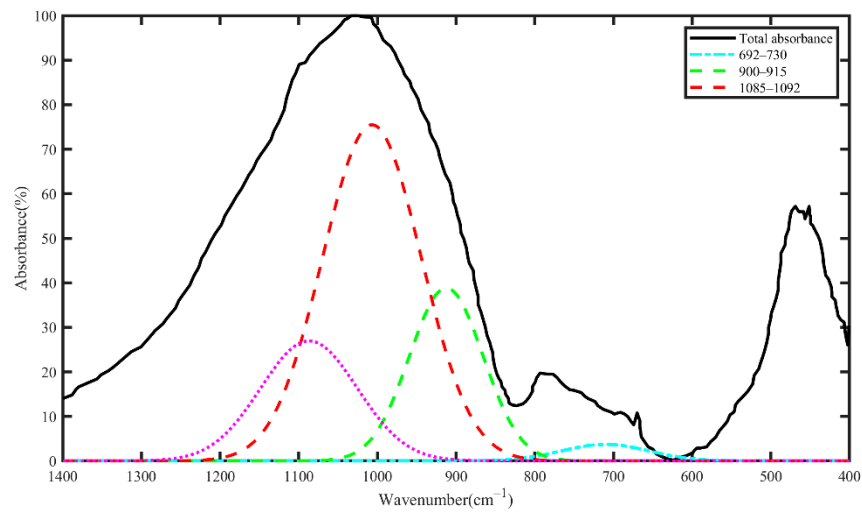


Figure 3. FTIR absorbance and Gaussian curves of active bonds in the FA sample.

Table 3. Reactive bond parameters and reactivity calculation of the FA sample.

Active Peak Center	Identified Bond	Relative Area (%)	Reactivity Coefficient	Active Concentration (%)
710.1	Al-O	1.37	2	2.74
912.5	Si-O-M	11.34	0.75	8.5
1007	(Si, Al)-O-Si	29.3	0.5	14.7
1087	(Si, Al)-O-Si	10.3	0.25	2.6
Total active concentration				28.54
Reactive surface area (m <sup>2</sup> /g)				0.144

### 3.2. Mass Change of Carbon-Cured Geopolymer Paste and the CO<sub>2</sub> Absorption Capacity

The mass change after oven heating shows the amount of evaporable water for NC samples. The evaporable water is measured as 18.1% of the initial mass of the specimen. The mass change for CO<sub>2</sub> cured sample is lower compared to NC samples because of CO<sub>2</sub> absorption (Figure 4). The reduction in mass change by increasing the curing time indicates more absorption of CO<sub>2</sub>.

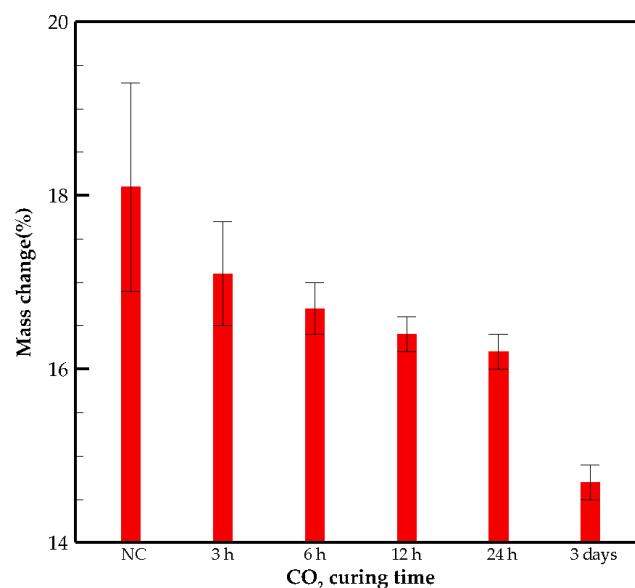


Figure 4. Mass change of samples after oven heating (%).

$\text{CO}_2$  uptake per mass of binder is calculated using Equation (3) and the average evaporable water in NC samples. The  $\text{CO}_2$  uptake at the early age occurs rapidly, and the rate of  $\text{CO}_2$  uptake for the first 3 h is about 0.46%/h. However, the  $\text{CO}_2$  uptake rate decreases between 3 and 24 h (Figure 4). This might be because of the presence of carbonated products that precipitate on the surface and in the pore structure, which hinders the diffusion of gaseous  $\text{CO}_2$  into the samples. By further  $\text{CO}_2$  curing, the gas molecules diffuse deeply into the matrix, and the precipitation rate of carbonated products increases.

The maximum capacity of  $\text{CO}_2$  absorption can be determined by the chemical composition of cementitious materials through Equation (4) [37,38]:

$$\text{CO}_2 = 0.785(\text{CaO} - 0.7\text{SO}_3) + 1.091\text{MgO} + 1.42\text{Na}_2\text{O} + 0.935\text{K}_2\text{O} \quad (4)$$

It should be noted that the above formula was suggested for OPC. Consequently, caution should be taken when using Equation (4) for alkali-activated materials [37]. Based on Equation (4), the maximum  $\text{CO}_2$  absorption capacity of the specimens is 21.23%. The maximum  $\text{CO}_2$  uptake after 3-day  $\text{CO}_2$  curing is approximately 5% from the test data, which indicates a major portion of the samples is not carbonated. Depending on the source of the fly ash, different values of  $\text{CO}_2$  uptake efficiency have been reported. Hernandez et al. proposed the aqueous mineralization of carbon dioxide in fly ash powder without addition of an activator and calculated a 2.6%  $\text{CO}_2$  uptake per tonne of fly ash [39]. Calcium hydroxide carbonation was considered the main reaction controlling the mineral sequestration of  $\text{CO}_2$ . The same reaction mechanism was considered by Mazzella et al. who obtained  $\text{CO}_2$  uptake at about 18 wt% fly ash by gas–solid carbonation treatment [40].

### 3.3. Efflorescence Measurement

$\text{CO}_2$  cured samples show a high amount of efflorescence. This phenomenon deteriorates both the appearance aesthetics and mechanical properties of AAMs. High amount of efflorescence is observed on the surfaces, especially on the top of the samples.

Regarding the titration test, only carbonate and hydroxide ions are observed, while bicarbonate ions are not detected. By measuring the concentration of carbonate ions, the weight of hydrated carbon dioxide in the solution is calculated. Figure 5 represents the  $\text{CO}_2$  uptake and its rate per mass of the paste versus curing time obtained from the titration test. The absorption rate of carbon dioxide indicates that in the early stages of curing, the paste has a high absorption capacity, while this potential decreases significantly over time.

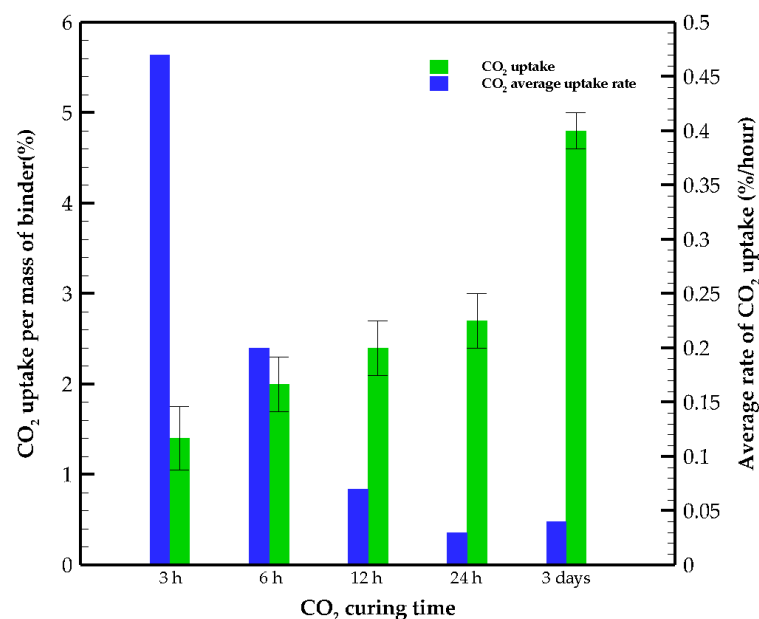
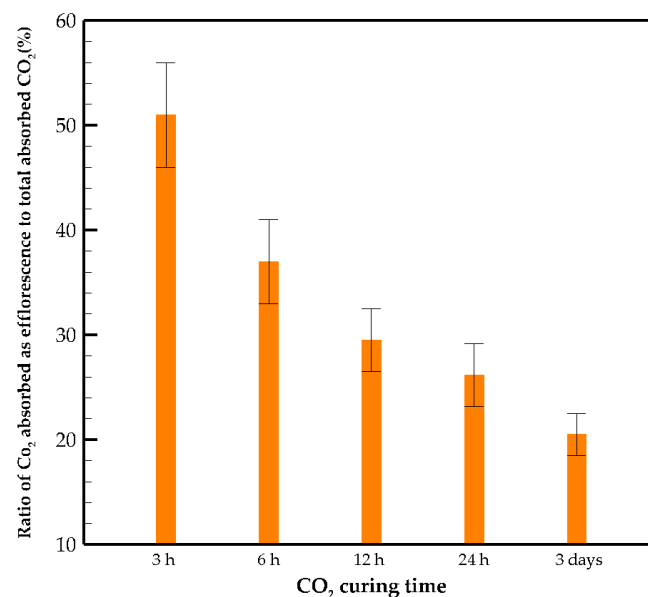


Figure 5.  $\text{CO}_2$  uptake per mass of FA and its average rate with respect to curing time for specimens.

The efficiency of CO<sub>2</sub> mineralization mentioned in the literature for aqueous carbonation and gas–solid carbonation is 82% and 74%, respectively [39,40]. These efficiencies are obtained for powder samples, while the CO<sub>2</sub> mineralization examined here is for the paste specimens. The efficiency ratios for 3 h, 6 h, 12 h, 24 h and 3 days specimens are obtained by dividing the CO<sub>2</sub> uptakes from Figure 5 by the total capacity of carbonation calculated from Equation (4), which are 6.6, 9.4, 11.3, 12.7 and 22.6%, respectively. The ratio of CO<sub>2</sub> absorbed as efflorescence to the total absorbed CO<sub>2</sub> shows the effectiveness of carbon curing (Figure 6). In the early age of carbonation, almost half of the carbonated products appear as efflorescence due to the existence of a high amount of free alkaline ions on the sample surface, while at longer curing times, more CO<sub>2</sub> is fixed in the matrix. The dissolution of CO<sub>2</sub> forms carbonic acid in the pore solution and may cause a reduction in the pH of the pore solution, which occurs in natural carbonation and hinders further progress of the reaction. In OPC, calcium hydroxide acts as a buffer and saturates the pore solution with Ca<sup>2+</sup> and OH<sup>-</sup>; consequently, the pH level of the pore solution stays above 12, which protects the steel reinforcement against corrosion. CO<sub>2</sub> buffer capacity significantly affects the carbonation resistance and can be represented as the ratio of water to reactive calcium oxide [10]. In severe cases, after the consumption of portlandite, the pH of the pore solution starts to decrease. By lowering the pH under 12.6, C-S-H, ettringite (AFt) and monosulfate (AFm) become unstable. Additionally, the protection layer of steel reinforcement disappears when the pH is less than 9.5, and eventually, calcium carbonates precipitate in the pore structure. In AAMs, carbonation occurs in a two-step process:

- (1) Precipitation of sodium carbonates and reduction in pH of the pore solution.
- (2) Consumption of calcium-rich products.



**Figure 6.** Percentage of CO<sub>2</sub> absorbed as efflorescence with respect to curing time.

The carbonation of AAMs, unlike OPC, depends on both the reactive CaO and Na<sub>2</sub>O content of the precursor [12]. In comparison to OPC, AAMs do not include portlandite and contain low amount of reactive calcium. The lack of portlandite results in the decalcification of C-A-S-H gel and the production of silica gel that might be engaged in the geopolymerization process and densify the AAMs' microstructure.

### 3.4. Compression Strength Results

The change of the 28 days' strength is monitored for NC and CO<sub>2</sub> cured samples in Figure 7. The CO<sub>2</sub> curing is found to be detrimental in all cases in comparison to NC samples. However, in 24 h and 3 days specimens, higher compressive strength was obtained



compared to 3 h, 6 h and 12 h samples. This is probably due to the existence of calcium carbonates in the pores and the participation of the produced silicates in the polymerization process. After a 12 h curing, CO<sub>2</sub> is absorbed as a stable carbonate product, such as calcium carbonate, with different morphologies, including calcite, aragonite and vaterite. Calcium silicates are mostly converted to calcium carbonates based on the following reaction in carbon-cured samples [15]:

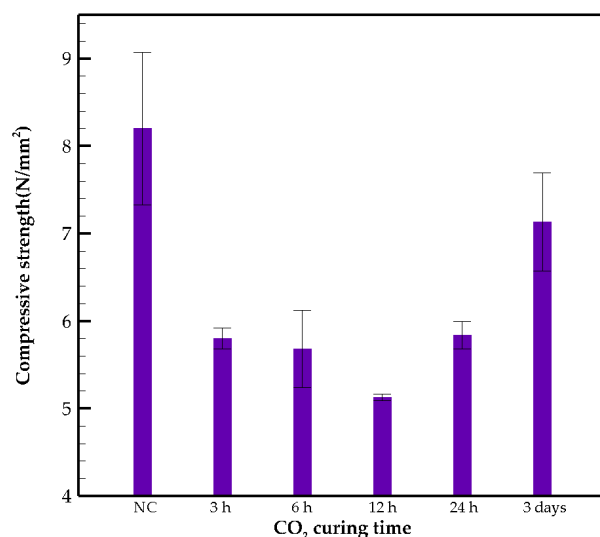


Figure 7. 28 days' compressive strength.

The produced silicate reacts with the silicate network in the geopolymer and improves the structure of the matrix. The polymerization of the aluminosilicate gel and increasing molar volume of products, which reduces the porosity, have been reported in previous literature [41,42]. Unlike OPC, where the production of calcium carbonate (CaCO<sub>3</sub>) is detrimental during carbonation, in GC, this phenomenon could have the opposite effect because the main structure in AAMs is constructed based on silicates and aluminates [15], and the additional SiO<sub>2</sub> produced through the reaction explained by Equation (5) might supply more reactive silica and enhance the geopolymerization process. This might be the reason for the increased strength in 24 h and 3 days samples. The presence of calcite in 24 h and 3 days specimens detected by XRD is further evidence that could explain this discrepancy in compressive strength results.

### 3.5. XRD Test Results

XRD analysis is conducted to analyze the products of CO<sub>2</sub> curing geopolymer with respect to the different curing durations (Figure 8). According to the XRD patterns, 24 h and 3 days samples are similar with respect to the identified minerals. The calcite peaks ( $2\theta = 29.6^\circ, 39.5^\circ, 43.6^\circ, 47.2^\circ$ ) [8] are detected in both samples. The presence of calcite, which precipitates in the pores, might be the reason for the increased strength after 24 h CO<sub>2</sub> curing. The formation of calcite and vaterite after one day in alkaline-activated blast furnace slag (BFSS) has also been reported in the literature [2]. Vaterite is unstable under accelerated carbonation and converts to calcite; however, the growth of calcite depends on the adequate supply of CO<sub>2</sub> and dissolution rate of Vaterite [2]. Gaylussite (Na<sub>2</sub>Ca(CO<sub>3</sub>)<sub>2</sub>·5H<sub>2</sub>O) is detected in both 24 h and 3 days samples. Natron is a carbonation product of low CO<sub>2</sub> concentration, and nahcolite is a carbonation product of high concentration of carbon dioxide [41]. In the obtained XRD patterns, nahcolite ( $2\theta = 30.58^\circ, 34.58^\circ, 40.84^\circ$ ) peaks might be overlapped with gaylussite peaks. In the initial steps of carbonation, vaterite is expected to form as a metastable polymorph of calcium carbonate [43,44]. Quartz, mullite

and hematite are identified in the samples as well [45]. In the presence of high humidity, vaterite crystallizes into calcite [46]. Besides the moisture content, the pH value of pore solution also contributes to the crystallization of vaterite. The pH value of pore solutions in AAMs after carbonation is usually above 9 in natural carbonation [47]. C(N)-A-S-H gel is thermodynamically less stable than C-S-H gel and is mainly amorphous, which causes different phase dissolution resulting from carbonation compared to OPC [48,49]. Pirssonite ( $\text{Na}_2\text{Ca}(\text{CO}_3)_2 \cdot 2\text{H}_2\text{O}$ ) and calcium disilicate ( $\text{CaSi}_2\text{O}_5$ ) are detected in 3 h, 6 h and 12 h NC samples.

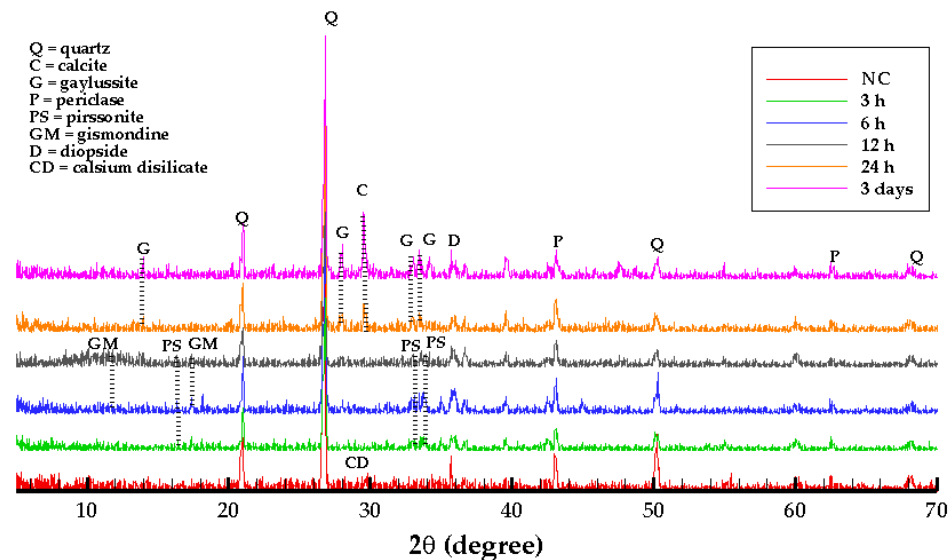


Figure 8. XRD diffractograms of non-carbonated and carbonated samples.

### 3.6. FTIR Test Results

The infrared spectra for NC and  $\text{CO}_2$  cured samples are shown in Figure 9. The absorption bands are divided into three regions, including water-related bonds, Si-O-Si bond and carbonate-related bonds [12]. In geopolymers, the amount of the non-bridging oxygen (NBO) depends on the  $\text{SiO}_2/\text{Na}_2\text{O}$  ratio of the activator solution [50]. When  $\text{SiO}_2/\text{Na}_2\text{O}$  ratio decreases, NBO decreases and contributes to lower silicon coordination with oxygen, such as the  $\text{SiQ}^2$  and  $\text{SiQ}^1$  units. Q stands for the oxygen bond formed with Si, and numbers 1 and 2 stand for the number of bonds formed. The geopolymerization process is recognized by Si-O-T (T: Si or Al) bonds with a wave number at  $950\text{ cm}^{-1}$  to  $1200\text{ cm}^{-1}$  and at  $650\text{ cm}^{-1}$  to  $750\text{ cm}^{-1}$ . Bands at  $450\text{ cm}^{-1}$  to  $1300\text{ cm}^{-1}$  are related to the Si-O-Si bond, and bands between  $1600\text{ cm}^{-1}$  and  $4000\text{ cm}^{-1}$  represent chemically bonded water. The stretching vibrational bonds of Si-O-Si are infrared active. The silicon coordination number, including  $\text{SiQ}^4$ ,  $\text{SiQ}^3$ ,  $\text{SiQ}^2$ ,  $\text{SiQ}^1$  and  $\text{SiQ}^0$ , is identified by wavenumbers at 1200, 1100, 950, 900 and  $850\text{ cm}^{-1}$ , respectively [35,43,50,51]. In all samples, it is seen that the absorption bands related to  $\text{Q}^3$  and  $\text{Q}^2$  are dominant.

The  $713\text{ cm}^{-1}$  absorption peak that appears in the 12 h, 24 h and 3 days samples shows the bending vibration of  $\text{CO}_3^{2-}$  in calcite and aragonite [2,43]. The increase in band intensity at this wavenumber can be considered as the condensation of aluminosilicate gel with a high amount of aluminum. The absorbance that appears between  $1400\text{ cm}^{-1}$  and  $1500\text{ cm}^{-1}$  is related to the stretching of  $\text{CO}_3^{2-}$  and represents the existence of calcite and vaterite [35,52,53]. It is seen that by increasing the  $\text{CO}_2$  curing time, the intensity of the band increases. At the early-age  $\text{CO}_2$  curing, the existence of aragonite and vaterite for NC, 3 h, 6 h samples is observed at  $1489\text{ cm}^{-1}$  and  $1490\text{ cm}^{-1}$ . The existence of this band for non-carbonated samples shows the effect of carbonation weathering. The presence of nahcolite ( $\text{NaHCO}_3$ ) is seen at band  $1450\text{ cm}^{-1}$ , and calcite is detected at band  $1419\text{ cm}^{-1}$  [12] for 12 h, 24 h and 3 days samples, which is consistent with the XRD results. As  $\text{CO}_2$  curing progresses, more crystallized  $\text{CaCO}_3$  forms. The out-of-plane bending mode

of the carbonates is located at  $875\text{ cm}^{-1}$  [35], which is only detected for 12 h, 24 h and 3 days samples.

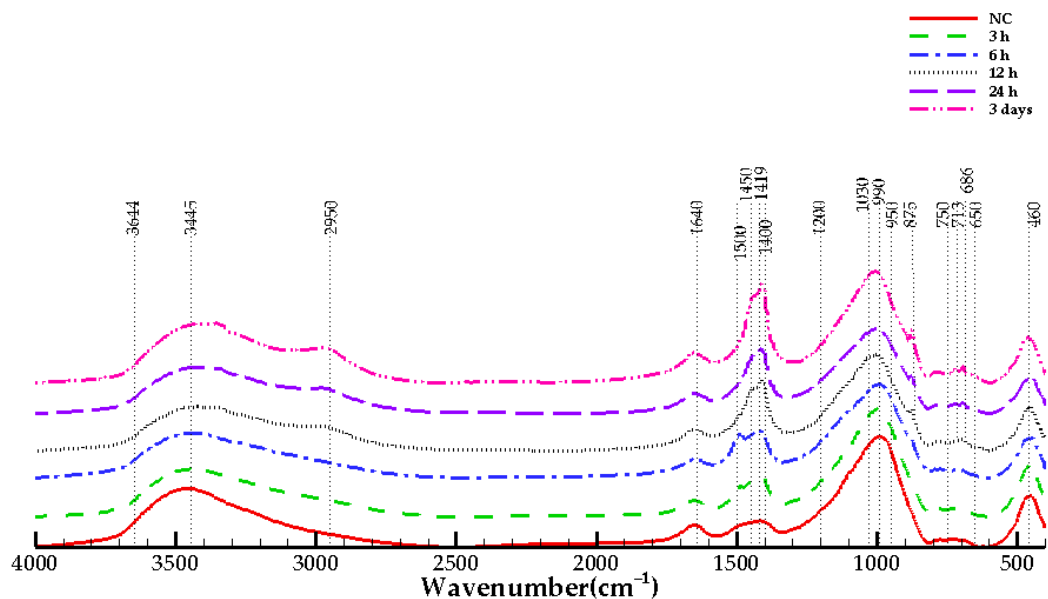


**Figure 9.** FTIR spectroscopy of NC and  $\text{CO}_2$  cured samples.

In 12 h, 24 h and 3 days samples, a peak close to  $2950\text{ cm}^{-1}$  is seen, which could possibly indicate the existence of vibrational bonds between carbon and hydrogen that has been detected in stearic acid [54]. The bending vibration of H-OH bonds appears in  $1640\text{ cm}^{-1}$ , which shows the existence of chemically bonded water [12,35]. It is seen that the peak is almost unchanged among all samples. The absorption at  $3445\text{ cm}^{-1}$  shows the stretching vibration of the O-H bond in bonded water [2]. The absorption of bonded water in calcium hydroxide appears at  $3644\text{ cm}^{-1}$  [2,55,56], which has low intensity.

### 3.7. TGA Test Results

The results of thermogravimetric analysis (TGA) and its derivative to temperature (DTG) are represented in Figure 10. In the NC sample, the predominant mass loss occurs below  $400\text{ }^\circ\text{C}$ . The change of mass between  $25\text{ }^\circ\text{C}$  and  $105\text{ }^\circ\text{C}$  shows the loss of evaporable water. The mass change from  $105\text{ }^\circ\text{C}$  to  $215\text{ }^\circ\text{C}$  shows the loss of bonded water in matrix and decomposition of C(N)-A-S-H gel [8]. The amount of C(N)-A-S-H gel decreases from NC samples to 3 days samples. The surface area under the DTG curves shows that  $\text{CO}_2$  cured samples have a lower amount of bonded water in their structure [35,57]. The peak at  $170\text{ }^\circ\text{C}$  is related to thermal decomposition of hydrotalcite [58]. The dehydration of pirssonite and gaylussite occurs at temperatures under  $250\text{ }^\circ\text{C}$  [59]. Natron is dehydrated at  $160\text{ }^\circ\text{C}$  [60] in  $\text{CO}_2$  cured samples, and the intensity of the peak reduces as curing progresses. The decomposition of total carbonated phases occurs in the range of  $400\text{ }^\circ\text{C}$  to  $800\text{ }^\circ\text{C}$  [35,42,61]. Amorphous calcium carbonate ( $\text{CaCO}_3$ ) decomposes at  $400\text{--}600\text{ }^\circ\text{C}$  [8]. Higher amount of crystalline  $\text{CaCO}_3$  is detected ( $600\text{--}750\text{ }^\circ\text{C}$  [8]) in the case of increased  $\text{CO}_2$  curing time [62]. However, the morphology of calcium carbonates in FA-based AAMs is more amorphous [12]. Regarding the literature, the crystallinity of polymorphs of calcium carbonates depends on many factors, including temperature, relative humidity, chemical composition of the binder and concentration of carbon dioxide [12,63].

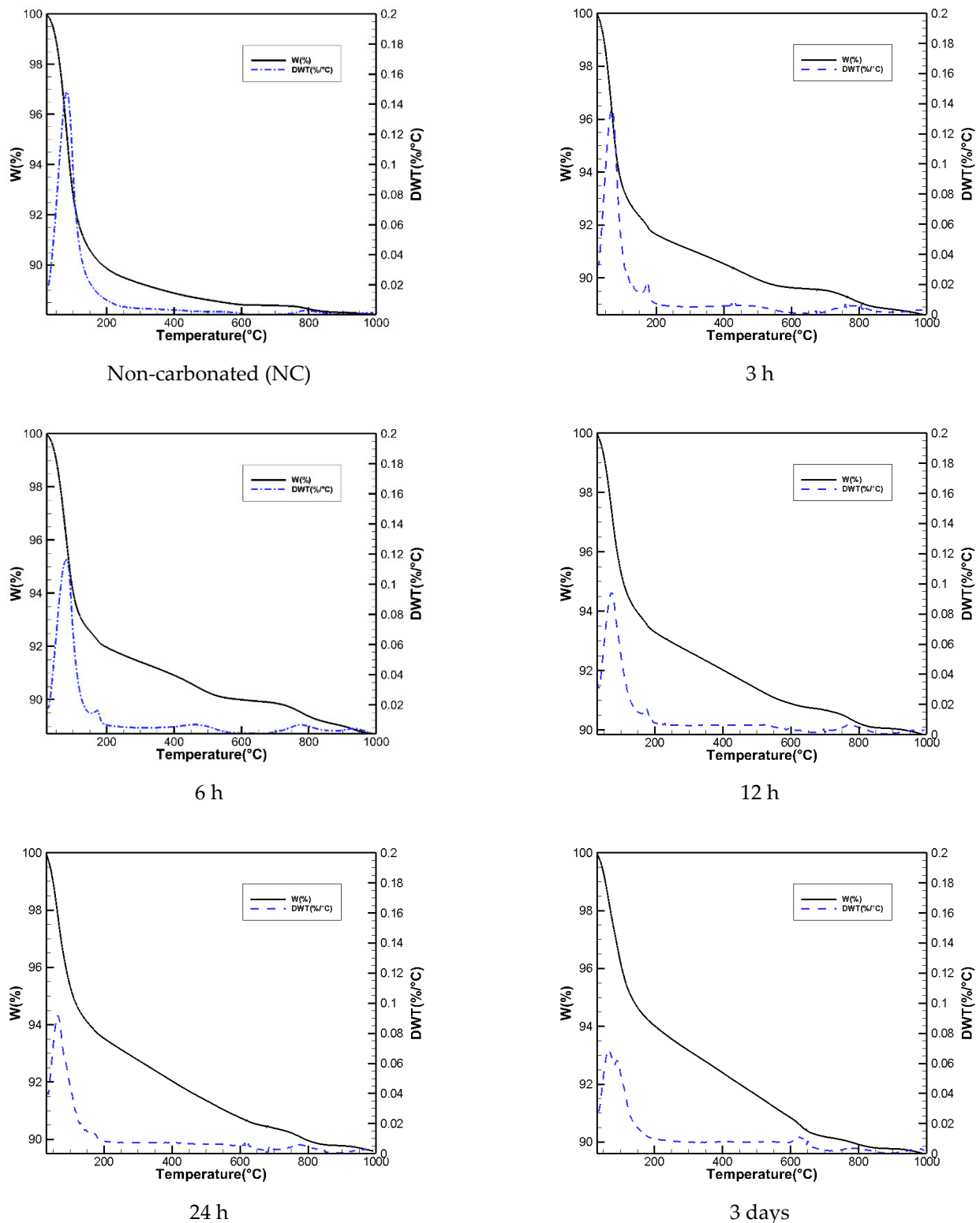


Figure 10. Thermogravimetric analysis results.

#### 4. Conclusions

In this study, the effect of CO<sub>2</sub> curing on low reactive fly ash alkali-activated pastes in the early ages was investigated. Five CO<sub>2</sub> curing times were applied on alkaline-activated FA samples in the presence of pure CO<sub>2</sub> under four-bar pressure. The following conclusions are drawn according to the experimental results:

- Curing time had a significant effect on the carbonation products and the amount of absorbed CO<sub>2</sub>. The maximum CO<sub>2</sub> uptake was obtained for the 3 days sample at 4.8 wt% fly ash, and the maximum efficiency was obtained at 22.6%.
- In short-term curing times, almost 50% of the absorbed carbon dioxide was efflorescence; however, by increasing the curing time, the absorbed CO<sub>2</sub> in the matrix increased in the form of insoluble and stable products.
- It was observed that carbon curing had a detrimental effect on the compressive strength in all specimens in comparison to the control sample. The presence of carbonic acid consumed the alkali and hydroxide ions in the pore solution, which lowered the pH of the pore solution and, consequently, hindered the progress of the geopolymerization reaction. At later ages of curing (after 24 h), the compressive strength started to rise slightly, which could be due to the presence of calcite and silica gel in the pore structure that was detected by XRD in 24 h and 3 days specimens.

**Author Contributions:** Conceptualization, M.Y. and P.H.; Funding acquisition, M.Y.; Investigation, P.H.; Methodology, M.Y.; Project administration, M.Y. All authors have read and agreed to the published version of the manuscript.

**Funding:** The research is funded by ND NSF EPSCoR.

**Institutional Review Board Statement:** Not applicable.

**Informed Consent Statement:** Not applicable.

**Data Availability Statement:** Data sharing not applicable.

**Conflicts of Interest:** The authors declare no conflict of interest.

## References

1. Thomas, R.J.; Peethamparan, S. Alkali-activated concrete: Engineering properties and stress–strain behavior. *Constr. Build. Mater.* **2015**, *93*, 49–56. [[CrossRef](#)]
2. Mei, K.; Gu, T.; Zheng, Y.; Zhang, L.; Zhao, F.; Gong, P.; Huang, S.; Zhang, C.; Cheng, X. Effectiveness and microstructure change of alkali-activated materials during accelerated carbonation curing. *Constr. Build. Mater.* **2021**, *274*, 122063. [[CrossRef](#)]
3. Zhang, D.; Ghouleh, Z.; Shao, Y. Review on carbonation curing of cement-based materials. *J. CO<sub>2</sub> Util.* **2017**, *21*, 119–131. [[CrossRef](#)]
4. Haselbach, L.M.; Thomle, J.N. An alternative mechanism for accelerated carbon sequestration in concrete. *Sustain. Cities Soc.* **2014**, *12*, 25–30. [[CrossRef](#)]
5. Lippiatt, N.; Ling, T.-C. Rapid hydration mechanism of carbonic acid and cement. *J. Build. Eng.* **2020**, *31*, 101357. [[CrossRef](#)]
6. Ohenoja, K.; Rissanen, J.; Kinnunen, P.; Illikainen, M. Direct carbonation of peat-wood fly ash for carbon capture and utilization in construction application. *J. CO<sub>2</sub> Util.* **2020**, *40*, 101203. [[CrossRef](#)]
7. Zhang, D.; Cai, X.; Shao, Y. Carbonation Curing of Precast Fly Ash Concrete. *J. Mater. Civ. Eng.* **2016**, *28*, 04016127. [[CrossRef](#)]
8. Yamazaki, Y.; Kim, J.; Kadoya, K.; Hama, Y. Physical and Chemical Relationships in Accelerated Carbonation Conditions of Alkali-Activated Cement Based on Type of Binder and Alkali Activator. *Polymers* **2021**, *13*, 671. [[CrossRef](#)]
9. Cui, H.; Tang, W.; Liu, W.; Dong, Z.; Xing, F. Experimental study on effects of CO<sub>2</sub> concentrations on concrete carbonation and diffusion mechanisms. *Constr. Build. Mater.* **2015**, *93*, 522–527. [[CrossRef](#)]
10. Leemann, A.; Nygaard, P.; Kaufmann, J.; Loser, R. Relation between carbonation resistance, mix design and exposure of mortar and concrete. *Cem. Concr. Compos.* **2015**, *62*, 33–43. [[CrossRef](#)]
11. Nedeljković, M.; Ghiassi, B.; van der Laan, S.; Li, Z.; Ye, G. Effect of curing conditions on the pore solution and carbonation resistance of alkali-activated fly ash and slag pastes. *Cem. Concr. Res.* **2019**, *116*, 146–158. [[CrossRef](#)]
12. Nedeljković, M.; Ghiassi, B.; Melzer, S.; Kooij, C.; van der Laan, S.; Ye, G. CO<sub>2</sub> binding capacity of alkali-activated fly ash and slag pastes. *Ceram. Int.* **2018**, *44*, 19646–19660. [[CrossRef](#)]
13. Li, Z.; Li, S. Effects of wetting and drying on alkalinity and strength of fly ash/slag-activated materials. *Constr. Build. Mater.* **2020**, *254*, 119069. [[CrossRef](#)]
14. Zhang, X.; Long, K.; Liu, W.; Li, L.; Long, W.-J. Carbonation and Chloride Ions' Penetration of Alkali-Activated Materials: A Review. *Molecules* **2020**, *25*, 5074. [[CrossRef](#)]
15. Ul Haq, E.; Padmanabhan, S.K.; Licciulli, A. In-situ carbonation of alkali activated fly ash geopolymer. *Constr. Build. Mater.* **2014**, *66*, 781–786. [[CrossRef](#)]
16. He, J.; Gao, Q.; Wu, Y.; He, J.; Pu, X. Study on improvement of carbonation resistance of alkali-activated slag concrete. *Constr. Build. Mater.* **2018**, *176*, 60–67. [[CrossRef](#)]

17. Arbi, K.; Nedeljković, M.; Zuo, Y.; Ye, G. A Review on the Durability of Alkali-Activated Fly Ash/Slag Systems: Advances, Issues, and Perspectives. *Ind. Eng. Chem. Res.* **2016**, *55*, 5439–5453. [[CrossRef](#)]
18. Amran, M.; Fediuk, R.; Murali, G.; Avudaiappan, S.; Ozbakkaloglu, T.; Vatin, N.; Karelina, M.; Klyuev, S.; Gholampour, A. Fly Ash-Based Eco-Efficient Concretes: A Comprehensive Review of the Short-Term Properties. *Materials* **2021**, *14*, 4264. [[CrossRef](#)]
19. Kassim, D.; Lamaa, G.; Silva, R.V.; de Brito, J. Performance Enhancement of Alkali-Activated Electric Arc Furnace Slag Mortars through an Accelerated CO<sub>2</sub> Curing Process. *Appl. Sci.* **2022**, *12*, 1662. [[CrossRef](#)]
20. Park, S.-M.; Jang, J.-G.; Kim, G.-M.; Lee, H.-K.; Park, S.-M.; Jang, J.-G.; Kim, G.-M.; Lee, H.-K. Strength Development of Alkali-Activated Fly Ash Exposed to a Carbon Dioxide-Rich Environment at an Early Age. *J. Korean Ceram. Soc.* **2016**, *53*, 18–23. [[CrossRef](#)]
21. Li, Z.; Xu, G.; Shi, X. Reactivity of coal fly ash used in cementitious binder systems: A state-of-the-art overview. *Fuel* **2021**, *301*, 121031. [[CrossRef](#)]
22. ASTM C618-19; Specification for Coal Fly Ash and Raw or Calcined Natural Pozzolan for Use in Concrete. ASTM International: West Conshohocken, PA, USA, 2019. [[CrossRef](#)]
23. ASTM C305-20; Practice for Mechanical Mixing of Hydraulic Cement Pastes and Mortars of Plastic Consistency. ASTM International: West Conshohocken, PA, USA, 2020. [[CrossRef](#)]
24. Huntzinger, D.N.; Gierke, J.S.; Kawatra, S.K.; Eisele, T.C.; Sutter, L.L. Carbon Dioxide Sequestration in Cement Kiln Dust through Mineral Carbonation. *Environ. Sci. Technol.* **2009**, *43*, 1986–1992. [[CrossRef](#)]
25. Pacheco-Torgal, F.; Shi, C.; Palomo, A. *Carbon Dioxide Sequestration in Cementitious Construction Materials*; Woodhead Publishing: Sawston, UK, 2018; ISBN 978-0-08-102447-8.
26. Wang, Y.; Liu, X.; Zhang, W.; Li, Z.; Zhang, Y.; Li, Y.; Ren, Y. Effects of Si/Al ratio on the efflorescence and properties of fly ash based geopolymer. *J. Clean. Prod.* **2020**, *244*, 118852. [[CrossRef](#)]
27. Zhang, D.; Shao, Y. Early age carbonation curing for precast reinforced concretes. *Constr. Build. Mater.* **2016**, *113*, 134–143. [[CrossRef](#)]
28. ASTM C566-19; Test Method for Total Evaporable Moisture Content of Aggregate by Drying. ASTM International: West Conshohocken, PA, USA, 2019. [[CrossRef](#)]
29. Xue, X.; Liu, Y.-L.; Dai, J.-G.; Poon, C.-S.; Zhang, W.-D.; Zhang, P. Inhibiting efflorescence formation on fly ash-based geopolymer via silane surface modification. *Cem. Concr. Compos.* **2018**, *94*, 43–52. [[CrossRef](#)]
30. Zhang, Z.; Provis, J.L.; Ma, X.; Reid, A.; Wang, H. Efflorescence and subflorescence induced microstructural and mechanical evolution in fly ash-based geopolymers. *Cem. Concr. Compos.* **2018**, *92*, 165–177. [[CrossRef](#)]
31. Najafi Kani, E.; Allahverdi, A.; Provis, J.L. Efflorescence control in geopolymer binders based on natural pozzolan. *Cem. Concr. Compos.* **2012**, *34*, 25–33. [[CrossRef](#)]
32. Yao, X.; Yang, T.; Zhang, Z. Compressive strength development and shrinkage of alkali-activated fly ash–slag blends associated with efflorescence. *Mater. Struct.* **2016**, *49*, 2907–2918. [[CrossRef](#)]
33. ASTM D3875-15; Test Method for Alkalinity in Brackish Water, Seawater, and Brines. ASTM International: West Conshohocken, PA, USA, 2017. [[CrossRef](#)]
34. C01 Committee; Test Method for Compressive Strength of Hydraulic Cement Mortars (Using 2-in. or [50-mm] Cube Specimens). ASTM International: West Conshohocken, PA, USA, 2020. [[CrossRef](#)]
35. Zhang, J.; Shi, C.; Zhang, Z. Effect of Na<sub>2</sub>O concentration and water/binder ratio on carbonation of alkali-activated slag/fly ash cements. *Constr. Build. Mater.* **2021**, *269*, 121258. [[CrossRef](#)]
36. Zhang, Z.; Wang, H.; Provis, J.L. Quantitative study of the reactivity of fly ash in geopolymerization by FTIR. *J. Sustain. Cem. Based Mater.* **2012**, *1*, 154–166. [[CrossRef](#)]
37. Ashraf, W. Carbonation of cement-based materials: Challenges and opportunities. *Constr. Build. Mater.* **2016**, *120*, 558–570. [[CrossRef](#)]
38. Fernández Bertos, M.; Simons, S.J.R.; Hills, C.D.; Carey, P.J. A review of accelerated carbonation technology in the treatment of cement-based materials and sequestration of CO<sub>2</sub>. *J. Hazard. Mater.* **2004**, *112*, 193–205. [[CrossRef](#)] [[PubMed](#)]
39. Montes-Hernandez, G.; Pérez-López, R.; Renard, F.; Nieto, J.M.; Charlet, L. Mineral sequestration of CO<sub>2</sub> by aqueous carbonation of coal combustion fly-ash. *J. Hazard. Mater.* **2009**, *161*, 1347–1354. [[CrossRef](#)] [[PubMed](#)]
40. Mazzella, A.; Errico, M.; Spiga, D. CO<sub>2</sub> uptake capacity of coal fly ash: Influence of pressure and temperature on direct gas-solid carbonation. *J. Environ. Chem. Eng.* **2016**, *4*, 4120–4128. [[CrossRef](#)]
41. Bernal, S.A.; Provis, J.L.; Walkley, B.; San Nicolas, R.; Gehman, J.D.; Brice, D.G.; Kilcullen, A.R.; Duxson, P.; van Deventer, J.S.J. Gel nanostructure in alkali-activated binders based on slag and fly ash, and effects of accelerated carbonation. *Cem. Concr. Res.* **2013**, *53*, 127–144. [[CrossRef](#)]
42. Shi, Z.; Shi, C.; Wan, S.; Li, N.; Zhang, Z. Effect of alkali dosage and silicate modulus on carbonation of alkali-activated slag mortars. *Cem. Concr. Res.* **2018**, *113*, 55–64. [[CrossRef](#)]
43. Zhang, J.; Shi, C.; Zhang, Z. Carbonation induced phase evolution in alkali-activated slag/fly ash cements: The effect of silicate modulus of activators. *Constr. Build. Mater.* **2019**, *223*, 566–582. [[CrossRef](#)]
44. Sarkar, A.; Mahapatra, S. Synthesis of All Crystalline Phases of Anhydrous Calcium Carbonate. *Cryst. Growth Des.* **2010**, *10*, 2129–2135. [[CrossRef](#)]

45. Nedeljković, M.; Šavija, B.; Zuo, Y.; Luković, M.; Ye, G. Effect of natural carbonation on the pore structure and elastic modulus of the alkali-activated fly ash and slag pastes. *Constr. Build. Mater.* **2018**, *161*, 687–704. [[CrossRef](#)]
46. Šauman, Z.; Lach, V. Long-term carbonization of the phases  $3\text{CaO}\cdot\text{Al}_2\text{O}_3\cdot 6\text{H}_2\text{O}$  and  $3\text{CaO}\cdot\text{Al}_2\text{O}_3\cdot\text{SiO}_2\cdot 4\text{H}_2\text{O}$ . *Cem. Concr. Res.* **1972**, *2*, 435–446. [[CrossRef](#)]
47. Bernal, S.A.; Provis, J.L.; Brice, D.G.; Kilcullen, A.; Duxson, P.; van Deventer, J.S.J. Accelerated carbonation testing of alkali-activated binders significantly underestimates service life: The role of pore solution chemistry. *Cem. Concr. Res.* **2012**, *42*, 1317–1326. [[CrossRef](#)]
48. Hidalgo, A.; Domingo, C.; Garcia, C.; Petit, S.; Andrade, C.; Alonso, C. Microstructural changes induced in Portland cement-based materials due to natural and supercritical carbonation. *J. Mater. Sci.* **2008**, *43*, 3101–3111. [[CrossRef](#)]
49. White, C.E.; Daemen, L.L.; Hartl, M.; Page, K. Intrinsic differences in atomic ordering of calcium (alumino) silicate hydrates in conventional and alkali-activated cements. *Cem. Concr. Res.* **2015**, *67*, 66–73. [[CrossRef](#)]
50. Dimas, D.; Giannopoulou, I.; Papias, D. Polymerization in sodium silicate solutions: A fundamental process in geopolymerization technology. *J. Mater. Sci.* **2009**, *44*, 3719–3730. [[CrossRef](#)]
51. Ye, H.; Cai, R.; Tian, Z. Natural carbonation-induced phase and molecular evolution of alkali-activated slag: Effect of activator composition and curing temperature. *Constr. Build. Mater.* **2020**, *248*, 118726. [[CrossRef](#)]
52. Zhang, Z.; Wang, H.; Provis, J.L.; Bullen, F.; Reid, A.; Zhu, Y. Quantitative kinetic and structural analysis of geopolymers. Part 1. The activation of metakaolin with sodium hydroxide. *Thermochim. Acta* **2012**, *539*, 23–33. [[CrossRef](#)]
53. Andersen, F.; Brečević, L. Infrared Spectra of Amorphous and Crystalline Calcium Carbonate. *ChemInform* **1992**, *23*. [[CrossRef](#)]
54. Qu, Z.Y.; Gauvin, F.; Wang, F.Z.; Liu, G.; Brouwers, H.J.H. Effect of hydrophobicity on autogenous shrinkage and carbonation of alkali activated slag. *Constr. Build. Mater.* **2020**, *264*, 120665. [[CrossRef](#)]
55. Lee, W.K.W.; van Deventer, J.S.J. Use of Infrared Spectroscopy to Study Geopolymerization of Heterogeneous Amorphous Aluminosilicates. *Langmuir* **2003**, *19*, 8726–8734. [[CrossRef](#)]
56. Van Jaarsveld, J.G.S.; Van Deventer, J.S.J.; Schwartzman, A. The potential use of geopolymeric materials to immobilise toxic metals: Part II. Material and leaching characteristics. *Miner. Eng.* **1999**, *12*, 75–91. [[CrossRef](#)]
57. Zuo, Y.; Nedeljković, M.; Ye, G. Coupled thermodynamic modelling and experimental study of sodium hydroxide activated slag. *Constr. Build. Mater.* **2018**, *188*, 262–279. [[CrossRef](#)]
58. Rey, F.; Fornés, V.; Rojo, J.M. Thermal decomposition of hydrotalcites. An infrared and nuclear magnetic resonance spectroscopic study. *J. Chem. Soc. Faraday Trans.* **1992**, *88*, 2233–2238. [[CrossRef](#)]
59. Johnson, D.R.; Robb, W.A. Gaylussite: Thermal properties by simultaneous thermal analysis. *Am. Mineral.* **1973**, *58*, 778–784.
60. Sharma, S.K.; Jotshi, C.K.; Kumar, S. Thermal stability of sodium salt hydrates for solar energy storage applications. *Sol. Energy* **1990**, *45*, 177–181. [[CrossRef](#)]
61. Kim, G.M.; Jang, J.G.; Naeem, F.; Lee, H.K. Heavy Metal Leaching,  $\text{CO}_2$  Uptake and Mechanical Characteristics of Carbonated Porous Concrete with Alkali-Activated Slag and Bottom Ash. *Int. J. Concr. Struct. Mater.* **2015**, *9*, 283–294. [[CrossRef](#)]
62. Šauman, Z. Carbonization of porous concrete and its main binding components. *Cem. Concr. Res.* **1971**, *1*, 645–662. [[CrossRef](#)]
63. Johannesson, B.; Utgenannt, P. Microstructural changes caused by carbonation of cement mortar. *Cem. Concr. Res.* **2001**, *31*, 925–931. [[CrossRef](#)]